Journal of the Iranian Chemical Society (2020) 17:1087–1101
https://doi.org/10.1007/s13738-019-01837-6

ORIGINAL PAPER

Catalytic behaviour of molybdenum-based zeolitic materials prepared by organic-medium impregnation and sublimation methods

Emna Mannei[1,2] · Faouzi Ayari[1,2] · Esther Asedegbega-Nieto[3] · Mourad Mhamdi[2,4] · Gérard Delahay[5]

Received: 31 July 2019 / Accepted: 16 December 2019 / Published online: 21 December 2019

Abstract

Molybdenum-exchanged ZSM-5 catalysts were tested in ethane ammoxidation into acetonitrile at 500 °C and at a very low contact time (0.08 s). The solids were prepared by sublimation, impregnation in CCl_4 and solid-state ion exchange methods. The hydration state of the zeolite strongly affected the nature of $MoCl_5$ and $Mo(CO)_6$ decomposition products and, therefore, the concentration of stabilized Mo species in the final catalysts. In effect, using dehydrated ZSM-5 zeolite, the sublimation of $MoCl_5$ led to the most active catalyst (TOF = 8.78 s^{-1}) due to the presence, essentially, of $[MoO_4]^{2-}$ (77%) and $[Mo_2O_7]^{2-}$ (10%) besides less-active crystalline MoO_3 (12%) and traces of heptamers. However, the impregnation and the solid-state ion exchange of $MoCl_5$ as well as the sublimation of $Mo(CO)_6$ led to less-active catalysts owing to the presence of inefficient MoO_3 oxide phase. In fact, moderate concentrations of crystalline MoO_3 should coexist with $[MoO_4]^{2-}$ species in order to activate C_2H_6 into C_2H_4 instead of enhancing the deep hydrocarbons' oxidation.

Keywords ZSM-5 zeolite · Sublimation · Impregnation · Ammoxidation

Introduction

Acetonitrile (AN) market has witnessed a significant growth over the past decade. In fact, a recent report entitled "*Acetonitrile Market: Global Industry Trends, Share, Size, Growth, Opportunity and Forecast 2019–2024*" published by *IMARC* Group estimates that the global AN market had reached 113 kt in 2018. However, this research report anticipates the market to reach 143 kt by 2024, exhibiting a compound annual growth rate (CAGR) of ~ 5% during 2019–2024 [1]. Such an annual growth rate can be accredited to the versatile application of AN as solvent for high-performance liquid chromatography [2] and intermediate in the synthesis of pyrimidine derivatives [3]. Nonetheless, due to its high dielectric constant ($\varepsilon = 35.85$ at 25 °C under 1 bar [4]), stability and ability to dissolve electrolytes, acetonitrile is also used in the manufacturing of batteries. In effect, the strong demand for lithium batteries, as a result of their growing usage in electronic devices, is further propelling the market growth [5]. As a matter of fact, the synthesis routes of AN as the main reaction product have been sought and an efficient atom economy could be achieved by using C2 substrates such as acetic acid [6], ethanol [7], ethylene [8] and ethane [9].

Electronic supplementary material The online version of this article (https://doi.org/10.1007/s13738-019-01837-6) contains supplementary material, which is available to authorized users.

✉ Emna Mannei
emna.mannei@fst.utm.tn

1 Laboratoire de développement chimique, galénique et pharmacologique des médicaments, Faculté de Pharmacie de Monastir, Université de Monastir, Rue Avicenne, 5000 Monastir, Tunisia

2 Laboratoire de chimie des matériaux et catalyse, Faculté des Sciences de Tunis, Université de Tunis El Manar, Campus universitaire Tunis El Manar, 2092 Tunis, Tunisia

3 Dpto. química inorgánica y química técnica, Facultad de Ciencias, Universidad Nacional de Educación a Distancia, Paseo Senda del Rey 9, 28040 Madrid, Spain

4 Institut Supérieur des Technologies Médicales de Tunis, Université de Tunis El Manar, 9 Avenue Docteur Zouhaier Essafi, 1006 Tunis, Tunisia

5 Institut Charles Gerhardt Montpellier, UMR 5253, CNRS–UM–ENSCM, Matériaux avancés pour la catalyse et la santé, ENSCM, 240 Avenue du Professeur Emile Jeanbrau, CS 60297, 34296 Montpellier Cedex 05, France

Ethane ammoxidation (Eq. 1) is an alternative route for the manufacture of AN. Indeed, all the commercially produced acetonitrile is obtained as a co-product from the ammoxidation of propylene into acrylonitrile (Eq. 2) over $Bi_9PMo_{12}O_{52}$-50 wt% SiO_2 material [10]:

$$C_2H_6 + NH_3 + 1.5O_2 \rightarrow CH_3CN + 3H_2O \quad (1)$$

$$CH_2 = CH{-}CHO + NH_3 + 0.5O_2 \rightarrow CH_2 = CH{-}CN + 2H_2O \quad (2)$$

Although no C_2H_6 ammoxidation process is as yet commercial, the advances in catalysis may make it an economic alternative for AN production in the near future [11]. In this context, we reported the successful application of beta zeolite modified with cobalt in ethane ammoxidation into AN at a contact time of 130 m*s* [12, 13]. Additionally to acetonitrile, the primary products in ethane ammoxidation over Co-exchanged beta zeolite are ethylene and CO_2 [12, 13]. Nevertheless, interesting results have been obtained at a very low contact time (80 ms) over molybdenum-exchanged ZSM-5 zeolites prepared by solid-state ion exchange, which consists of mixing the zeolite and the precursor in a mortar and subsequently heating the powder under helium stream at 500 °C for 12 h [9, 14].

Interestingly, several methods were developed to introduce Mo into zeolites, which include sublimation [15–17], impregnation [18, 19] and sonochemical method [20]. The latter method is considered to be costly, while the inexpensive solid-state ion exchange (SSIE) has a number of advantages, e.g. achieving a high metal exchange degree in one step. However, SSIE also has major disadvantages since, on heating, some precursors undergo complex changes [21]. For example, the thermal decomposition of $MoCl_5$ in the presence of zeolite may be accompanied by the melting of the molybdenum salt, involving the participation of several intermediates and products ($MoOCl_4$, $MoOCl_3$, MoO_3 and $MoO_2(OH)_2$ [22]).

Although wetness impregnation has been found to be an interesting method, the use of an excess of solution is not preferred. Indeed, Mo^{6+} ion forms in aqueous medium the stable tetraoxidomolybdate(2–) complex ($[MoO_4]^{2-}$) which is easily protonated and polymerized, giving rise to very complex systems of simultaneous equilibria [23, 24]. As for the sublimation method (i.e. chemical vapour deposition, CVD), the primary disadvantage lies in the properties of the precursors. Ideally, the precursors need to be volatile at near-room temperatures. Nevertheless, this is not trivial for a number of elements in the periodic table although the use of metal-organic precursors (e.g. $Mo(CO)_6$ [25]) has eased this situation. The precursors used for sublimation or CVD can also be highly toxic ($Ni(CO)_4$), explosive (B_2H_6) or corrosive ($SiCl_4$), while the by-products can be hazardous (H_2, HF or CO) [26].

Alternative exchange methods have to be investigated in order to introduce Mo into zeolites including sublimation (e.g. *g*$MoCl_5$, and $Mo(CO)_6$ which evaporates at low temperature, ca. 200 °C [25]) and organic-medium impregnation (e.g. $MoO_2(C_5H_7O_2)_2$ in CH_2Cl_2 [27] and $MoCl_5$ in $CH_2Cl{-}CH_2Cl$ [28]).

In view of the great practical importance of Mo-exchanged zeolites, sublimation and organic-medium impregnation are expeditious alternative methods to prepare solid catalysts with definable structure and composition. In this work, we prepared Mo-exchanged ZSM-5 zeolite catalysts by solid-state ion exchange (solid–solid interface: $MoCl_{5(s)}$ + hydrated zeolite), sublimation (gas–solid interface: dehydrated zeolite + $MoCl_{5(g)}$ and hydrated zeolite + $Mo(CO)_{6(s)}$) and organic-medium impregnation (solid–liquid interface: dehydrated zeolite + $MoCl_{5(s)}$ dissolved in CCl_4). We have used several spectroscopic techniques (e.g. X-ray photoelectron and optical spectroscopy) in order to characterize the prepared catalysts, namely those active in ethane ammoxidation into acetonitrile.

Experimental

Catalysts preparation

The Mo-containing solids, denoted as Mo-P, were prepared according to the following protocols:

Solid-state ion exchange

This method consists of mixing the NH_4^+-ZSM-5 zeolite powder (Si/Al = 26, Zeolyst) with the desired quantity of $MoCl_5$ (Mo/Al molar ratio = 1, i.e. 6 wt% of Mo) in a mortar. The mixture was subsequently heated under helium stream (30 cm^3 min^{-1}) from room temperature to 500 °C (heating rate 2 °C min^{-1}) and then isothermally treated for 12 h at 500 °C. The prepared solid was stored and labelled as Mo-SSIE where SSIE stands for solid-state ion exchange.

Impregnation in organic medium

For organic-medium impregnation method, solid $MoCl_5$ was dispersed in anhydrous CCl_4 (wt $MoCl_5$/wt $CCl_4 = 2 \times 10^{-3}$) under continuous stirring for 1 h at room temperature. The mixture was then transferred in a round-bottom flask containing the NH_4^+-ZSM-5 zeolite powder (Si/Al = 26) and connected to a rotary evaporator. It is worth mentioning that the zeolite was previously dehydrated under vacuum at room temperature for 12 h. The contact of the dehydrated zeolite with $MoCl_5/CCl_4$ mixture was performed by the rotation of the flask for 3 h inside a water bath heated at 70 °C. After the evacuation of the solvent, the mixture (6 wt% of Mo) was

dried in an oven at 100 °C for 12 h and then treated under helium stream at 500 °C (2 °C min^{-1}, 30 cm^3 min^{-1}) for 12 h. Thereafter, it was treated under pure O_2 (30 cm^3 min^{-1}) at 500 °C (2°C min^{-1}) during 3 h before being stored and labelled as Mo-IMP, where IMP stands for impregnation.

Exchange by sublimation

Two different precursors were used for the exchange by sublimation: $MoCl_5$ and $Mo(CO)_6$. Starting from $MoCl_5$, we used a specific reactor (Scheme 1) in order to avoid the hydrolysis of the metallic precursor during the in-situ dehydration of the zeolite.

Firstly, the NH_4^+-ZSM-5 zeolite powder (Si/Al = 26) was dehydrated at 550 °C under helium (30 cm^3 min^{-1}) for 10 h. Subsequently, the reactor was cooled to 50 °C and an excess of salt was introduced (22 wt%, i.e. 7.2 wt% of Mo). The reactor was then heated under argon to 550 °C (2 °C min^{-1}) and was kept for 12 h at the same temperature. The prepared sample was labelled as Mo-SUB where SUB stands for sublimation.

Starting from $Mo(CO)_6$ (see Scheme 2), the exchange consists of mixing the fresh NH_4^+-ZSM-5 zeolite powder (Si/Al = 26) with the desired quantity of $Mo(CO)_6$ (6 wt% of Mo) in a mortar. The mixture was transferred in a Teflon liner that is sealed and placed in the oven at 100 °C for 12 h. Following the sublimation, the liner was cooled and the obtained powder was heated under helium stream (30 cm^3 min^{-1}) between room temperature and 500 °C (2 °C min^{-1}) and then isothermally treated at 500 °C for 12 h. The obtained material was labelled as Mo-CVD where CVD stands for chemical vapour deposition.

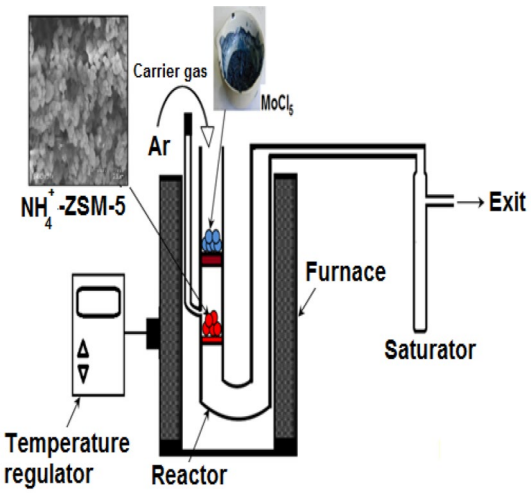

Scheme 1 The set-up used for the exchange of Mo into zeolite by $MoCl_5$ sublimation

Catalysts characterization

The different characterization techniques including inductively coupled plasma optical emission spectrometry (ICP-OES), energy-dispersive X-ray (EDX), thermal analysis coupled to mass spectrometry (TA/MS), nitrogen adsorption–desorption at − 196 °C, X-ray photoelectron spectroscopy (XPS), ^{27}Al magic angle spinning nuclear magnetic resonance (^{27}Al MAS NMR), X-ray diffraction (XRD), temperature-programmed reduction under hydrogen (H_2-TPR), temperature-programmed desorption of ammonia (NH_3-TPD), diffuse reflectance infrared Fourier-transform spectroscopy (DRIFTS) and UV/visible diffuse reflectance spectroscopy (UV/Vis DRS) were previously described [9, 14, 22, 24, 29] and reported in the electronic supplementary material.

Catalytic tests

Gas-phase ammoxidation was carried out at 500 °C using a catalyst weight $m = 200$ mg and the following gas composition: 10% C_2H_6, 10% NH_3, 10% O_2 and 70% He. The

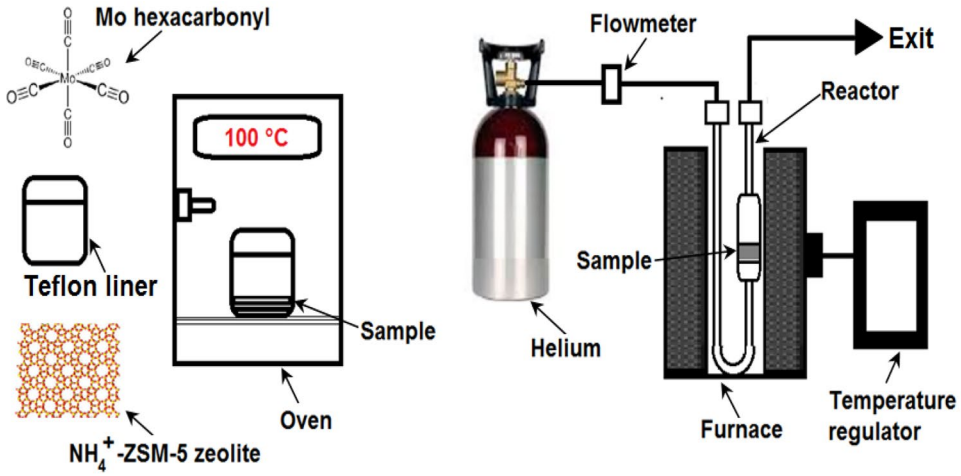

Scheme 2 Exchange of Mo into NH_4^+-ZSM-5 by sublimation of $Mo(CO)_6$ (denoted as chemical vapour deposition in order to discard the ambiguity with the sublimation of $MoCl_5$)

total flow rate was maintained at 100 cm^3 min^{-1} which corresponds to a contact time equal to 80 m*s*. The outlet gases were analysed by two chromatographic units (flame ionization and thermal conductivity detectors). The reaction products are essentially AN, C_2H_4 and CO_2. However, insignificant amounts of CO, CH_4 and NO by-products were also produced but were not included in the calculations.

The conversion (Eq. 3), selectivity (Eq. 4) and activity (Eq. 5) were defined as follows:

$$\text{Ethane conversion } \left(X_E\right) : X_E = \frac{\sum_i y_i n_i}{y_E n_E + \sum_i y_i n_i} \times 100 \quad (3)$$

where i stands for AN, C_2H_4 and CO_2.

$$\text{Selectivity of product } P_i \left(i = \text{AN, } C_2H_4 \text{ and } CO_2\right) : S_i = \frac{y_i n_i}{\sum_i y_i n_i} \times 100 \quad (4)$$

Here, y_i and y_E are the mole fractions of product P_i (AN, C_2H_4 and CO_2) and reactant C_2H_6, respectively, while n_i and n_E are the number of carbon atoms in each molecule of product P_i and reactant C_2H_6, respectively.

Activity of P_i product (Ac_i), i.e. the rate of P_i formation, is:

$$Ac_i\left(\text{mol s}^{-1}\text{ g}^{-1}\right) = \frac{\text{Hydrocarbon flow } \left(\text{cm}^3\text{ s}^{-1}\right) \times X_E \times S_i}{\text{Molar volume } \left(\text{STP, cm}^3\text{ mol}^{-1}\right) \times 10^4 \times m\text{ (g)}} \quad (5)$$

The turnover frequency (TOF), i.e. the activity per each Mo specie molecule, is determined as follows (Eq. 6):

$$\text{TOF } \left(\text{s}^{-1}\right) = \frac{Ac_i\ \left(\text{mol s}^{-1}\text{g}^{-1}\right)}{\text{Amount of Mo specie by gram of sample } \left(\text{mol g}^{-1}\right)} \quad (6)$$

Previously, we used the TOF concept in order to classify several catalytic systems in terms of activity recorded under steady-state conditions [12–14].

Results

Chemical and thermal analyses

The chemical analyses results obtained by ICP and EDX are compiled in Table 1.

According to Table 1, the sample prepared by the sublimation of $Mo(CO)_6$ (i.e. Mo-CVD solid) exhibited a significant metal weight loss (50%) which could be originated from the evaporation of $Mo(C{\equiv}O)_6$ precursor either inside the Teflon liner (in the oven) or during the thermal post-treatment. In effect, our thermal analysis results (unpublished work) revealed that the complete evaporation of Mo hexacarbonyl precursor occurred between 50 and 125 °C. However, in the case of Mo-SSIE solid, the Mo weight loss (49%) would originate from the evaporation of $MoCl_5$ decomposition products (e.g. $MoO_2(OH)_2$) during the solid-state ion exchange. Certainly, the formation of gaseous $MoO_2(OH)_2$ complex takes places during the decomposition of $MoCl_5$ into MoO_3 which reacts with H_2O molecules (issued from the zeolite dehydration) according to Eq. 7 [24, 29, 30]:

$$MoO_{3(s)} + H_2O_{(g)} = MoO_2(OH)_{2(s)} = MoO_2(OH)_{2(g)} \quad (7)$$

If compared with solid-state ion exchange, the loss of molybdenum over Mo-IMP solid is less pronounced due to lack of water molecules in the medium (i.e. the reaction in Eq. 7 is less displaced to the right side). In fact, the totality of water molecules was evacuated below 50 °C as revealed by the evolution of the MS fragment intensity of H_2O (red curve in Fig. 1).

In the case of Mo-SUB solid (Table 1), we noticed a significant metal loss (76%) despite the use of an excess of Mo during the preparation procedure (7.2 instead of 6 wt%). The effect of water on the metal weight loss will be thoroughly dealt with in the Discussion section.

Table 1 ICP and EDX results

	Si/Al[a]	Mo[b]	Mo wt loss (%)[c]	Al[b]
NH_4^+-ZSM-5	27.01	–	–	1.54
Mo-SSIE	24.46	3.06	49	1.34
Mo-IMP	24.15	5.43	10	1.56
Mo-SUB	25.67	1.80	76	1.63
Mo-CVD	25.15	3.00	50	1.41

[a]mol/mol, determined by ICP

[b]wt%, average of five values determined by EDX

[c]$[(Mo_{theoret.} - Mo_{EDX.})/Mo_{theoret.}] \times 100$

Textural and XPS analyses

The textural analysis results, i.e. BET (S_{BET}) and microporous (S_{micro}) areas, microporous (V_{micro}) and porous (V_p) volumes, are compiled in Table 2.

Generally, the areas and the volumes relative to NH_4^+-ZSM-5 zeolite decrease upon the exchange evidencing that metallic clusters clogged the channels and made some pores inaccessible to N_2 molecules. However, the micropore blocking effect [14] was estimated by the calculation of the normalized microporous area given in Eq. 8:

$$\text{Normalized } S_{\text{micro}} = \frac{S_{\text{micro}} \text{ sample}}{S_{\text{micro}}\text{zeolite} \times (1 - y)} \quad (8)$$

Here, y stands for the Mo amount present at the surface, i.e. determined by EDX.

According to Table 2 (last column), Mo-CVD solid exhibited the lowest normalized S_{micro} value (0.64 vs. 1 for NH_4^+-ZSM-5) which indicates a pronounced obstruction of the zeolite micropores. In order to understand such a phenomenon, we performed XPS analysis over the solids which exhibited the highest and the lowest normalized S_{micro} values, i.e. Mo-SSIE and Mo-CVD, respectively. The results are compiled in Fig. 2 and Table 3 (see also Fig. S1 in electronic supplementary material).

In the Mo 3*d* XP spectrum of Mo-CVD solid (Fig. 2a), two sets of Mo 3*d* doublets representing Mo^{6+} in bulky MoO_3 (binding energy (BE) at 233.5 and 237.0 eV) and Mo^{6+} in MoO_x moieties (BE at 232.4 and 235.2 eV) were observed. Moreover, the XP spectrum of Mo-SSIE solid exhibited the same sets of doublets (see the positions in Fig. S1).

When compared with Mo-SSIE, the concentration of Mo at the surface of Mo-CVD solid is lower (Table 3) as also revealed by the intensities of the XPS doublets in Fig. 2b.

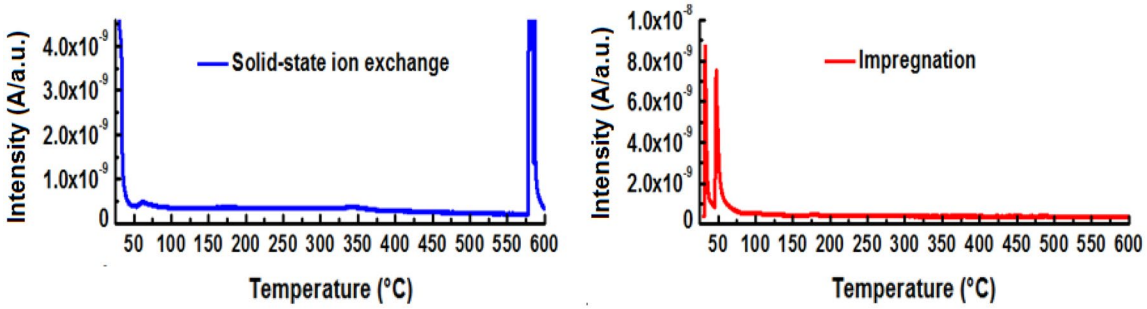

Fig. 1 Evolution of the signal intensity of H_2O^+ MS fragment during the thermal treatment of $MoCl_5/NH_4^+$-ZSM-5 mixtures prepared under solid-state ion exchange and impregnation conditions

Table 2 Textural analysis results

	S_{BET} ($m^2\ g^{-1}$)	S_{micro} ($m^2\ g^{-1}$)	V_p ($cm^3\ g^{-1}$)	V_{micro} ($cm^3\ g^{-1}$)	Normalized S_{micro}
NH_4^+-ZSM-5	367	291	0.21	0.13	1.00
Mo-SSIE	354	232	0.19	0.10[a]	0.82
Mo-IMP	336	204	0.19	0.09	0.74
Mo-SUB	381	218	0.23	0.10	0.76
Mo-CVD	269	182	0.17	0.08	0.64

[a]See electronic supplementary material, page S3

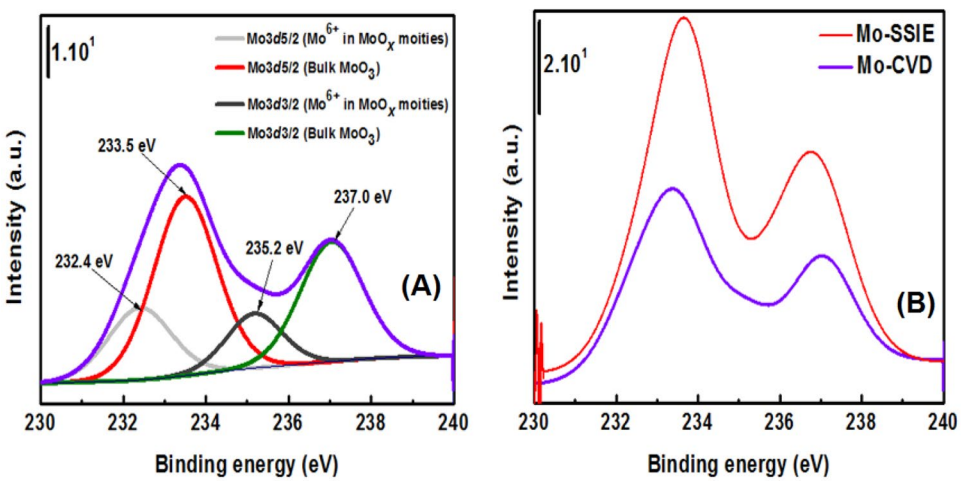

Fig. 2 **a** Deconvolution of the XP spectrum of Mo-CVD solid and **b** XP spectra of Mo-SSIE and Mo-CVD solids

Table 3 XPS analysis results

	Position (eV)	% wt conc.	% of bulk MoO_3	% of MoO_x species[c]
Mo-CVD			71.2[a]	28.8
Si 2*p*	105.26	50.64		
Mo 3*d*	233.15	4.25		
Al 2*p*	77.03	2.97		
C 1*s*	282.84	2.36		
Mo-SSIE			81.8[b]	18.2
Cl 2*p*	198.96	3.78		
Si 2*p*	105.02	43.61		
Mo 3*d*	233.69	4.83		
Al 2*p*	77.40	2.45		
C 1*s*	283.04	6.86		

[a]Areas of peaks at 233.5 and 237.0 eV divided by the area of Mo 3*d* doublet

[b]Areas of peaks at 233.7 and 236.9 eV divided by the area of Mo 3*d* doublet

[c]100%–% of bulk MoO_3

This is likely explained by the diffusion of Mo into the inner pores of Mo-CVD solid as previously reported for Mo/ZSM-5 [31] and Cr/ZSM-5 [8] systems. Nevertheless, Mo-CVD solid loaded low amounts of MoO_3 at the surface (71.2 vs. 81.8% for Mo-SSIE solid) which would explain the significant drop in the normalized S_{micro} value (Table 2).

Structural studies by ^{27}Al MAS NMR and XRD

The ^{27}Al MAS NMR spectra of selected Mo-P solids and NH_4^+-ZSM-5 zeolite are illustrated in Fig. 3.

The NMR spectrum of NH_4^+-ZSM-5 zeolite exhibited a peak at ca. ~ 55 ppm ascribed to the four-coordinate Al framework, while the very weak signal at ~ 0 ppm is attributed to the extra-framework octahedral Al centres [14].

The NMR spectrum of Mo-SSIE solid revealed a strong increase in the intensity of the peak at 0 ppm, while the peak situated at 56 ppm slightly decreases in intensity which proves some preservation of the zeolite structure (see also the Al wt% values determined by EDX at the surface, Table 1). Similar phenomenon, denoted as reversible dealumination, was previously described by Iglesia and coworkers [32] as well as our group [9] over Mo/ZSM-5 solids.

It is well known that the zeolite has a very regular structure with a restricted range of T–O–T angles (here, T represents an individual SiO_4 or AlO_4 tetrahedron) [33]. Lippmaa et al. [34] reported the following relation (Eq. 9) between the T–O–T angle (θ') and the ^{27}A1 isotropic chemical shift (δ_{cs}) for zeolites:

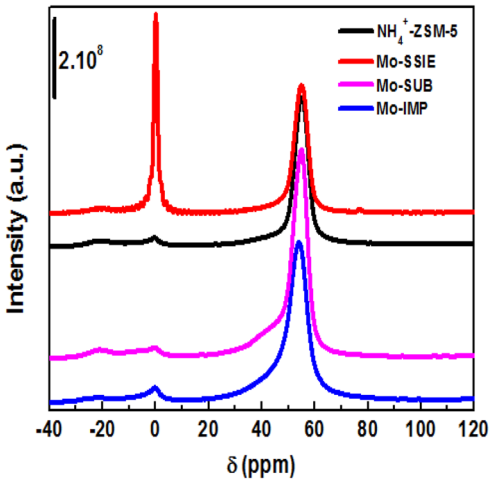

Fig. 3 ^{27}Al NMR spectra of Mo-SSIE, Mo-SUB, Mo-IMP solids and the corresponding support

$$\delta_{cs}(A1) = -0.50\,\theta' + 132\ (\text{ppm}) \tag{9}$$

From the NMR spectra compiled in Fig. 3, the θ' values were calculated and then compiled in Table 4.

According to Table 4, the introduction of Mo by impregnation in organic medium considerably modified the Si − Ô − Al angle value (155.9° vs. 154.1° for the rest of catalysts) since CCl_4 molecules (kinetic diameter $d = 5.4$ Å [35]) are able to diffuse during impregnation throughout the zeolite channels (dimension ~ 6 Å [30, 36]). In effect, a similar trend was reported by Fyfe et al. [37] with different organic molecules such as acetylacetone ($d = 5.6$ Å [38]), benzene ($d = 5.8$ Å [39]), pyridine ($d = 5.4$ Å [40]) and *p*-xylene ($d = 5.8$ Å [39]).

The XRD patterns of Mo-P solid and the corresponding support are presented in Fig. 4.

It is possible to calculate the unit-cell volume of the orthorhombic MFI zeolite ($a \neq b \neq c$, $\alpha = \beta = \gamma = 90°$) by XRD ($V = a \times b \times c$). Effectively, by choosing the appropriate *Miller* indexes, the unit-cell parameters could be determined by the formula in Eq. 10 [9]:

$$d_{(hkl)} = \frac{1}{\sqrt{\frac{h^2}{a^2} + \frac{k^2}{b^2} + \frac{l^2}{c^2}}} \tag{10}$$

Table 4 T–O–T angle (θ') determined from ^{27}Al NMR spectra of NH_4^+-ZSM-5 reference material and selected Mo-P solids

	δ_{cs} (ppm)	θ' (°)
NH_4^+-ZSM-5	55.1	153.9
Mo-SSIE	55.0	154.1
Mo-IMP	54.1	155.9
Mo-SUB	55.0	154.1

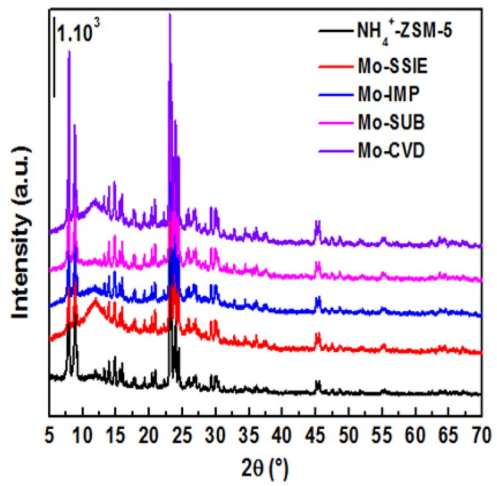

Fig. 4 XRD patterns of NH_4^+-ZSM-5 zeolite and Mo-P solids

In this context, the diffraction planes having $h = k = 0$ and $l \neq 0$ allow the determination of c, while the planes with h or $k = 0$ and $l \neq 0$ allow the determination of b or a. As a matter of fact, we selected the following planes (002), (012) and (312) in order to determine d_{hkl} from Bragg's law. The results are compiled in Tables 5 and S1.

The expansion [41] and the contraction [9] of the zeolite's lattice were previously studied by XRD. According to Table 5, the unit-cell volume of Mo-IMP is higher than those of Mo-SSIE, Mo-SUB and Mo-CVD solids which corroborates the NMR results.

In this study, the XRD patterns of Mo-P solids exhibit narrowed and well-defined diffraction lines similar to those of ZSM-5 zeolite [14] evidencing that the crystallinity is maintained upon the thermal treatment. Moreover, the diffractograms of the prepared materials do not show the lines ascribed to α-MoO_3 which indicates the absence of oxide crystallites with sizes above 20 nm [30].

In Fig. 4, we noticed also a broad baseline peak at low 2θ values in the diffractograms of Mo-SSIE and Mo-CVD solids which would probably be ascribed to an amorphous phase (see Fig. 2 in [30]).

Table 5 Crystallographic parameters and unit-cell volume relative to Mo-P and NH_4^+-ZSM-5 solids

Sample	a (Å)	b (Å)	c (Å)	V (Å^3)
NH_4^+-ZSM-5	20.07	20.28	13.35	5434 [9]
Mo-SSIE	20.04	20.16	13.37	5401 [9]
Mo-SUB	20.05	20.07	13.38	5384
Mo-CVD	20.12	19.97	13.39	5380
Mo-IMP	20.05	20.26	13.35	5423

H_2-TPR study

The TPR profiles of Mo-P solids are depicted in Fig. 5.

The TPR profile of Mo-SUB solid exhibits a shoulder at 450 °C attributed to the reduction of MoO_3 into MoO_2 [30]. However, the small shoulder centred at 700 °C would correspond to the reduction of MoO_2 into metallic molybdenum [30]. It is worth to note that the reduction of the zeolite dehydroxylation products as well as the evaporation of MoO_2 would take place at temperatures above 700 °C. As a matter of fact, the interpretation of the high-temperature region is very complicated and its discussion is not of interest in the present work.

When compared with Mo-SUB, the TPR profile of Mo-CVD solid shows an increase in the intensity of the peak ascribed to the reduction of MoO_3 with the subsequent shift of the temperature towards the right (from 450 to 470 °C). However, for Mo-IMP and Mo-SSIE solids, the reduction of MoO_3 occurs, respectively, at 495 and 515 °C, while tetrahedral Mo^{6+} ions were reduced at 595 °C. Apparently, the reduction temperature of MoO_3 oxide increases with the increase in the interactions developed with the support as depicted in the following sequence: Mo-SUB < Mo-CVD < Mo-Imp < Mo-SSIE.

NH_3-TPD and DRIFTS studies

The NH_3-TPD profiles of Mo-P solids and the corresponding support are shown in Fig. 6.

The NH_3-TPD profile of H^+-ZSM-5 zeolite and Mo-P solids exhibited a broad desorption peak between 100 and ~ 300 °C ascribed to weakly physisorbed ammonia molecules [42]. The intensity of this peak (denoted as low-temperature peak) depended on the operatory conditions

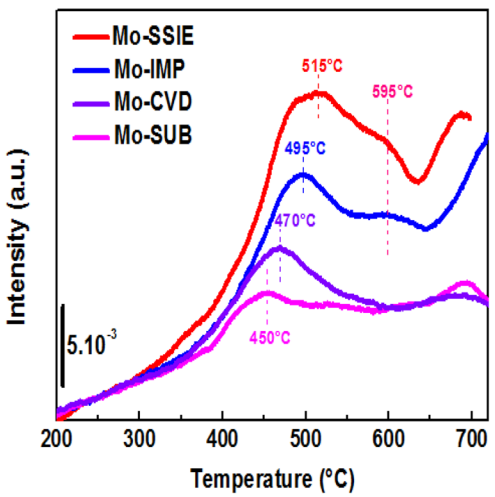

Fig. 5 TPR profiles of Mo-P solids

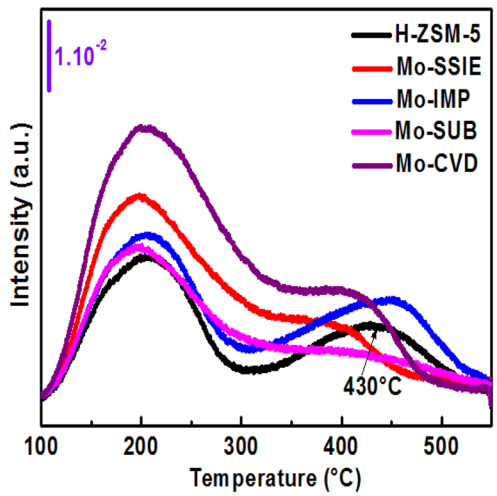

Fig. 6 NH_3-TPD profiles of Mo-containing solids and the corresponding support

[42], and hence, its contribution in the total acidity will be omitted. The NH_3-TPD profile of H^+-ZSM-5 zeolite showed a second peak centred at 430 °C which corresponds to the ammonia desorption from strong acid sites [9].

Sarv et al. [43] reported that the framework of ZSM-5 zeolite contains two strong Brønsted acid sites denoted as *b* and *b*′. However, in our TPD study, it is not possible to decompose the TPD profile of H^+-ZSM-5 into two peaks between 300 and 550 °C since the desorption process depends on kinetics, re-adsorption and diffusion phenomena. As a matter of fact, the deconvolution of the different TPD profiles into Gaussian curves should be performed by taking into consideration the presence of only one high-temperature desorption peak. Figure 7 represents the deconvolution of TPD profiles of Mo-P solids, while Table 6 summarizes the quantitative study results.

According to Figs. 6 and 7 as well as Table 6, the introduction of molybdenum modified the shape of the NH_3-TPD profile of the support due to the consumption of strong acidic sites and the generation of a moderate acidity. Specifically, Mo-IMP solid exhibited the lowest percentage of medium acidic site (46%), while the rest of the solids exhibited quasi-similar percentages of medium and strong acid sites.

The DRIFT spectra of the prepared solids and the zeolite support are presented in Fig. 8.

The DRIFT spectrum of the zeolite support exhibits two characteristic bands at 3595 and 3731 cm^{-1}, respectively, assigned to the vibration of Brønsted acid sites (Si–O^+H–Al) and the terminal silanol groups (Si–OH) [9]. The exchange of Mo into zeolite induces an attenuation of the 3595 cm^{-1} band's intensity evidencing that a fraction of Mo ions was deeply exchanged with Brønsted acid sites. In particular, the

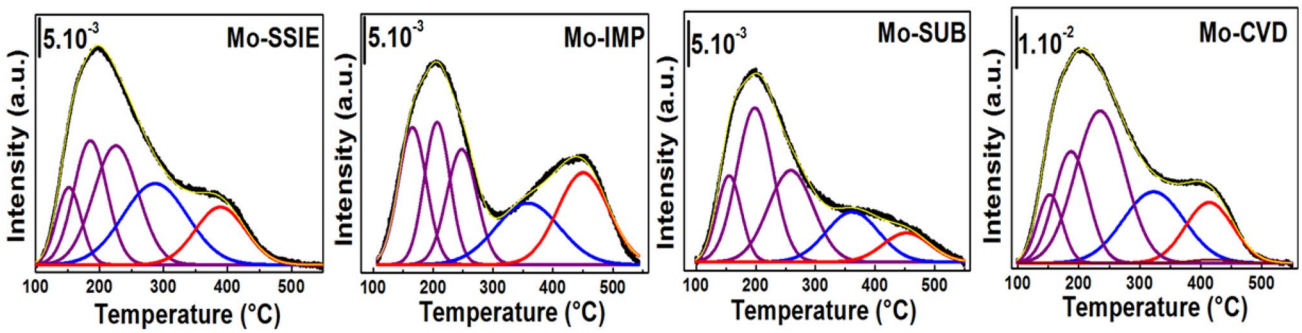

Fig. 7 Deconvolution of the NH_3-TPD profiles of Mo-containing solids

Table 6 NH_3-TPD results

		H^+-ZSM-5	Mo-SSIE [9]	Mo-IMP	Mo-SUB	Mo-CVD
T (°C)	$T^a_{\text{low-acidic}}$	N.D.[a]	152|186|226	165|207|248	155|198|258	153|187|235
	$T^b_{\text{medium-acidic}}$	–	286	358	362	323
	$T^c_{\text{strong-acidic}}$	423	386	450	452	414
Acidity ($mmolg^{-1}$)	NH^b_3	–	0.17	0.11	0.07	0.20
	NH^c_3	0.21 [9]	0.10	0.13	0.04	0.13
% of acidity[b]	Medium	–	63	46	64	61
	Strong	100	37	54	36	39

[a]Not determined

[b] $\left[NH^{c\text{ or }b}_3 \Big/ \left(NH^b_3 + NH^c_3\right)\right] \times 100$

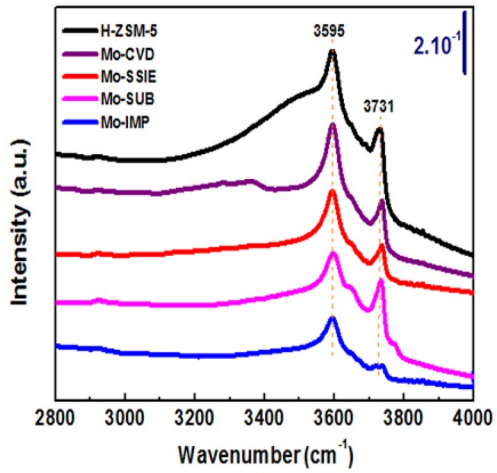

Fig. 8 DRIFT spectra of Mo-P solids and the corresponding support

spectrum of Mo-IMP solid revealed the significant decrease in the 3731 cm^{-1} band's intensity which could be explained by the grafting of Mo with silanol groups.

Optical properties: DRS study

Using the optical spectroscopy data, we explored the absorption band gap using the Schuster–Kubelka–Munk function (Eq. 11) and Eqs. (12) and (13) [14, 44]:

$$F(R_\infty) = \frac{(1-R_\infty)^2}{2R_\infty} \tag{11}$$

$$F(R_\infty) = \frac{(h\nu - E_g)^n}{h\nu} \tag{12}$$

$$[F(R_\infty) \times h\nu]^{\frac{1}{n}} = h\nu - E_g \tag{13}$$

Here, R_∞ is the diffuse reflectance of an infinitely thick sample, n is an exponent which takes the values of 2, 3, 1/2 and 3/2 for indirect allowed, indirect forbidden, direct allowed and direct forbidden transitions, respectively, $h\nu$ is the photon energy and E_g is the optical energy gap of the material [14, 44]. Plotting $[F(R_\infty)\times h\nu]^{1/n}$ ($n=2$ [14]) versus $h\nu$ and extrapolating to $[F(R_\infty)\times h\nu]^{0.5}=0$ yield the E_g value.

Figure 9 represents the deconvolution of the optical absorption spectra of the different solids (for the spectrum of Mo-SSIE solid, see Ref. [14]). We used Origin 8.0 (Microcal Software Inc., USA) in order to decompose the spectra into Gaussian peaks (for more details, see Ref. [14]).

The spectra of Mo-SUB and Mo-IMP solids revealed the presence of four $O^{2-} \rightarrow Mo^{6+}$ charge transfer bands assigned to MoO_3, $[Mo_7O_{24}]^{6-}$, $[Mo_2O_7]^{2-}$ and $[MoO_4]^{2-}$ (respectively, grey-, navy-, wine- and purple-coloured curve) [14, 45]. Nevertheless, the spectrum of Mo-CVD solid does not reveal the presence of the band ascribed to $[MoO_4]^{2-}$, while Mo-SSIE solid [14] contains only MoO_3 and $[Mo_2O_7]^{2-}$.

The concentration of MoO_3, $[Mo_7O_{24}]^{6-}$, $[Mo_2O_7]^{2-}$ and $[MoO_4]^{2-}$ species in each sample was determined by using the formula given in Eq. 14:

$$C_{Mo} = A_{Mo} \times k'_{Mo} \tag{14}$$

here A_{Mo} is the band's area of each Mo specie (obtained by the deconvolution in Fig. 9), while k' stands for the absorption coefficient. In our previous work [14], we determined the absorption coefficient of each Mo specie (see page 627 in Ref. [14]) to be 8.45×10^{-5}, 0.31×10^{-5}, 3.22×10^{-5} and 2.71×10^{-3} mol g^{-1} $(a.u.)^{-1}$, respectively, for MoO_3, $[Mo_7O_{24}]^{6-}$, $[Mo_2O_7]^{2-}$ and $[MoO_4]^{2-}$.

Table 7 summarizes the corresponding quantitative study results, while Table 8 represents the amount and the molar fraction of each Mo moiety.

According to the UV/Vis study results, Mo-P solids contain very low amounts of polymolybdates. However,

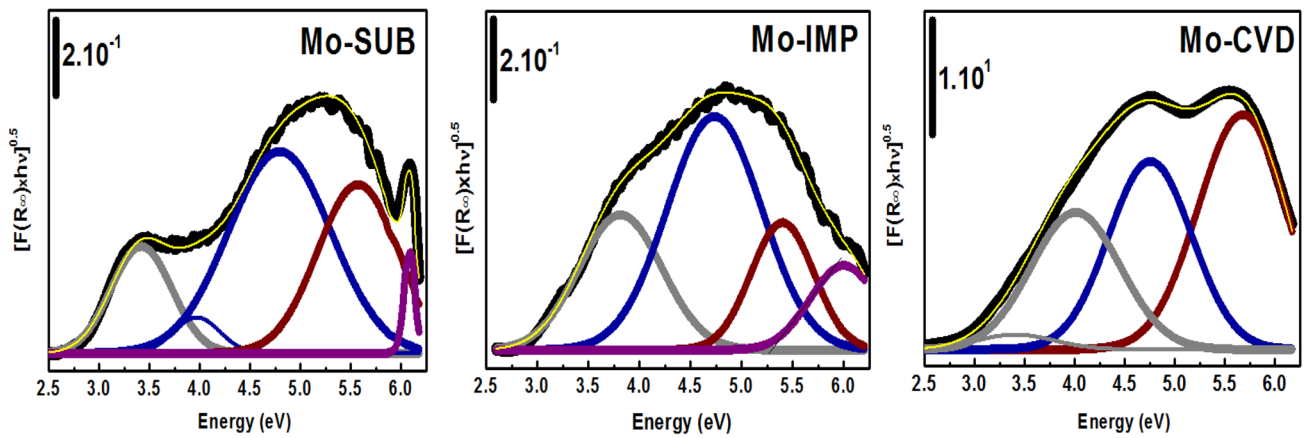

Fig. 9 Optical absorption spectra of Mo-SUB, Mo-IMP and Mo-CVD solids

Mo-SUB and Mo-IMP solids contain essentially monomeric species (77 and 92%, respectively), while Mo-SSIE and Mo-CVD samples contain only MoO_3 and $[Mo_2O_7]^{2-}$ moieties.

Catalytic results

Table 9 illustrates the catalytic behaviour of the prepared materials in ethane ammoxidation into acetonitrile (Eq. 1) at 500 °C. It is worth to mention that NH_4^+-ZSM-5 zeolite support does not exhibit any activity in the studied reaction (and therefore the results are not included in Table 9), while the rest of the catalysts are stable under the reaction conditions even after several hours on stream. On the other hand, the reproducibility tests do not reveal any significant change in activity.

The data compiled in Table 9 indicate a distinguishable difference in catalytic activity. For example, Mo-SSIE and Mo-CVD exhibited similar low activity towards ethylene formation (0.30 µmol s^{-1} g^{-1}), while the highest value was recorded over Mo-SUB catalyst ($Ac_{C_2H_4}$ = 0.62 µmol s^{-1} g^{-1}). Interestingly, Mo-SUB catalyst exhibited the highest selectivity towards ethylene (32%), while Mo-CVD and Mo-IMP solids led to the highest S_{CO_2} values (45 and 20%, respectively).

To compare the activity of Mo species in different catalysts, turnover frequency values (TOF, ethane molecule converted to ethylene or to acetonitrile per one Mo moiety and per second) were calculated using Eq. 6. The results are compiled in Table 10.

We believe that the intrinsic activity of a given Mo specie (either MoO_3 or $[Mo_2O_7]^{2-}$ or $[MoO_4]^{2-}$) should be the same in all catalysts. Nevertheless, the data compiled in Table 10 clearly evidenced that Mo species exhibit quite different activity with respect not only to different preparation methods but also to the different Mo moieties present in each catalyst. Such a discrepancy has been previously reported by Wichterlová and co-workers [46, 47]. In our recent work [14], we reported that synergistic effects and interactions may exist either between reactant (C_2H_6/C_2H_6) or

Table 7 Edge energy (E_g) values relative to each Mo specie and the area of the corresponding band

Sample	Edge energy value (E_g, eV) (values between brackets correspond to the area[a])				
	$[MoO_4]^{2-}$	$[Mo_2O_7]^{2-}$	$[Mo_7O_{24}]^{6-}$	MoO_3	Mo total amount (mol g^{-1})[b]
Mo-SSIE	–	4.20 (2.45)	–	2.85 (1.87)	3.20×10^{-4}
Mo-SUB	5.90 (0.045)	4.73 (0.47)	3.73 (0.77)	2.84 (0.22)	1.88×10^{-4}
Mo-IMP	5.33 (0.186)	4.75 (0.26)	3.75 (0.72)	2.97 (0.37)	5.68×10^{-4}
Mo-CVD	–	4.72 (2.33)	3.81 (1.74)	2.96 (1.50)	3.13×10^{-4}
α-MoO_3[c]	–	–	–	2.88 (2.78)	–

[a]Obtained by deconvolution of the spectra in Fig. 9

[b]Determined by EDX

[c]Ref. [14]

Table 8 Amount of each Mo moiety expressed in µmol g^{-1} (value between brackets: the corresponding molar fraction in %). Last column: the total amount of Mo moieties (µmol g^{-1})

	MoO_3	$[Mo_2O_7]^{2-}$	$[Mo_7O_{24}]^{6-}$	$[MoO_4]^{2-}$	$MoO_3+[Mo_2O_7]^{2-}+[Mo_7O_{24}]^{6-}+[MoO_4]^{2-}$
Mo-SSIE	158.0 (67)	78.9 (33)	–	–	237
Mo-SUB	18.6 (12)	15.1 (10)	2.4 (traces)	122.0 (77)	158
Mo-IMP	31.3 (6)	8.4 (traces)	2.2 (traces)	504 (92)	546
Mo-CVD	126.8 (61)	75 (36)	5.4 (traces)	–	207

Table 9 Catalytic behaviour of the prepared catalysts in C_2H_6 ammoxidation at 500 °C

Catalyst	X_E (%)	S (%)			Ac_{CH_3CN} (µ mol s^{-1} g^{-1})	$Ac_{C_2H_4}$ (µ mol s^{-1} g^{-1})
		CH_3CN	C_2H_4	CO_2		
Mo-SSIE	9.0	87	9	4	3.00	0.30
Mo-IMP	8.3	72	8	20	2.20	0.25
Mo-SUB	5.2	61	32	7	1.18	0.62
Mo-CVD	6.2	42	13	45	0.96	0.30

Table 10 Ethane ammoxidation: TOF values at 500 °C

	MoO_3	$[Mo_2O_7]^{2-}$	$[MoO_4]^{2-}$	$TOF([Mo_2O_7]^{2-}) + TOF([MoO_4]^{2-})$
TOF (s^{-1}): ethylene activity				
Mo-SSIE	0.19	0.38	–	0.38
Mo-IMP	0.80	–	0.05	0.05
Mo-SUB[a]	3.33	4.11	0.51	4.62
Mo-CVD	0.24	0.40	–	0.40
TOF (s^{-1}): acetonitrile activity				
Mo-SSIE	1.90	3.80	–	3.80
Mo-IMP	7.03	–	0.44	0.44
Mo-SUB[a]	6.43	7.81	0.97	8.78
Mo-CVD	0.76	1.28	–	1.28

[a]Under the assumption that the synergistic effects and the interactions between $[MoO_4]^{2-}$ and $[Mo_2O_7]^{2-}$ are negligible

intermediate (C_2H_4/C_2H_4 or $CH_3–CH_2–NH_2/CH_3–CH_2–NH_2$ or $C_2H_4/CH_3–CH_2–NH_2$) molecules during ammoxidation. In other words, if the active and/or inactive sites are too juxtaposed, the interactions between reactants and/or intermediates take place, leading to a discrepancy in individual TOF values.

In order to classify the catalysts in terms of catalytic activity, the TOF relative to ($[Mo_2O_7]^{2-} + [MoO_4]^{2-}$) is calculated in Table 10. In effect, we discarded MoO_3 and $[Mo_7O_{24}]^{6-}$ from the TOF calculation as the first specie may be either active (crystalline) or inactive (amorphous) [9, 14], while the second one exists at low concentrations (Table 8).

According to the TOF values compiled in Table 10, the specific activity of Mo-P catalysts towards ethylene formation (Eq. 15) increases in the following sequence: Mo-IMP < Mo-SSIE and Mo-CVD < Mo-SUB. However, the activity in ethane ammoxidation (Eq. $1 = \sum$ Eqs. 15–17) increases in the following sequence: Mo-IMP < Mo-CVD < Mo-SSIE < Mo-SUB:

$$C_2H_6 + O_2 \rightarrow C_2H_4 + H_2O \quad (15)$$

$$C_2H_4 + NH_3 \rightarrow CH_3CH_2NH_2 \quad (16)$$

$$CH_3CH_2NH_2 + O_2 \rightarrow CH_3CN + 2H_2O \quad (17)$$

Discussion

Theoretically, the diffusion of the trigonal-bipyramidal $MoCl_5$ molecule (kinetic diameter is 5.9 Å [22]) throughout the channels of the microporous NH_4^+-ZSM-5 zeolite (channel dimensionality: 5.3 × 5.6 and 5.1 × 5.5 Å [48]) requires a driving force, i.e. a specific thermal activation. Nevertheless, in reality, during the thermal treatment of the fresh zeolite under inert gas, water molecules evolve (Eq. 18), which modify the structure and the geometry of $MoCl_5$:

$$\left[NH_4^+ - ZSM - 5\right] x\ H_2O = NH_4^+ - ZSM - 5 + x\ H_2O \quad (18)$$

In fact, it has been demonstrated (see the graphical abstract of Ref. [22]) that the thermal treatment of pure $MoCl_5$ under helium stream led to the formation of $MoOCl_4$ and $MoOCl_3$ decomposition intermediates, while, in the presence of NH_4^+-ZSM-5 zeolite, pure $MoCl_5$ was decomposed into $MoOCl_4$ and $MoO_2(OH)_2$. Consequently, in this study, the hydration state of the used zeolite was the focus of our attention.

Starting from anhydrous $MoCl_5$, we used a fresh (humid) zeolite sample for exchanging molybdenum in the solid–solid interface, i.e. during solid-state ion exchange. However, the exchange in the solid–liquid interface by impregnation was carried out with a dehydrated zeolite sample and anhydrous $MoCl_5$ dissolved in CCl_4. Dehydrated CCl_4 was chosen in order to form the same decomposition intermediate as obtained during the solid-state ion exchange (i.e. $MoOCl_4$). In fact, electron-rich CCl_4 molecule oxidizes Mo^VCl_5 into $Mo^{VI}OCl_4$ as revealed by our TA/MS results (not shown). Nevertheless, the exchange at the solid–gas interface using sublimation of anhydrous $MoCl_5$ was performed also with dehydrated zeolite sample. In these conditions, $MoCl_5$ would be transformed in the absence of water into the volatile $MoOCl_4$ (between 75 and 200 °C [22]) and then into gaseous $MoOCl_3$ (at 313 °C [22]). The chemical vapour deposition is a combined preparation method which consists of reacting the hydrated zeolite and the volatile $Mo(CO)_6$, firstly in the solid–gas and then in the solid–solid interface. In the Teflon liner, the evaporation of $Mo(CO)_6$ occurs (Eq. 19), while during the thermal post-treatment, adsorbed $Mo(CO)_6$ (Eq. 20) losses C≡O molecules (Eq. 21) as revealed by the evolution of the signal intensity of CO^+ MS fragment (see Fig. S2). It is important to note that $Mo(CO)_6$ molecule has a significant size (the distance

between opposite O atoms is 6.4 Å [49], see Scheme S1) and is therefore adsorbed at the zeolite surface instead of diffusing throughout the channels. On the other hand, the use of hydrated zeolite is necessary in order to avoid the formation of Mo(0) (Eq. 22) at the detriment of MoO_x species (Eq. 23):

$$Mo(CO)_{6(s)} = Mo(CO)_{6(g)} \quad (19)$$

$$Mo(CO)_{6(g)} = Mo(CO)_{6(ads)} \quad (20)$$

$$Mo(CO)_{6(ads)} \rightarrow Mo(0) + 6CO_{(g)} \quad (21)$$

$$Mo(CO)_{6(ads)} + \text{dehydrated zeolite} \rightarrow Mo(0) + \text{dehydrated zeolite} \quad (22)$$

$$Mo(CO)_{6(ads)} + \text{hydrated zeolite} \rightarrow MoO_x \cdots \text{zeolite} \quad (23)$$

Prior to the SSIE, there is a partial transfer of H_2O molecules from the hydrated NH_4^+-ZSM-5 zeolite to the anhydrous $MoCl_5$ in the agate mortar. However, during the exchange at the solid–solid interface, the hydrated salt ($MoCl_5{\cdot}xH_2O$) is transformed into $MoOCl_{4(g)}$ and then into MoO_3 [22]. This later oxide reacts with H_2O issued from the zeolite hydration (Eq. 18) and forms the volatile $MoO_2(OH)_{2(g)}$ species (Eq. 7) leading to a significant Mo weight loss (49%, Table 1).

Based on the optical properties studied by UV/Vis DRS (Table 8), residual MoO_3 over Mo-SSIE solid represents 67% of the total Mo, while the remaining 33% of Mo exists in the dimeric form (78.9 µmol g^{-1}) reducible at 595 °C (Fig. 5). As a matter of fact, this solid does not contain monomeric nor heptameric species. However, the acidity measurement revealed that the formation of dimeric species was accompanied by the consumption of Brønsted acid sites (see the NH_3-TPD results in Fig. 6 and Table 6 as well as the attenuation of the DRIFTS band's intensity at 3595 cm^{-1} in Fig. 8). The residual band at 3595 cm^{-1} in Fig. 8 would belong to the vibrations of residual Brønsted acid sites (peak at 356 °C, Table 6). Apparently, the consumption of a fraction of Brønsted acid sites was accompanied by the formation of a medium acidic site (63%, Table 6) which evolves ammonia at 286 °C.

According to XPS results (Table 3), the surface of Mo-SSIE solid contains low amounts of $[Mo_2O_7]^{2-}$ species (18.2%). However, residual MoO_3 (reduced under H_2 at 515 °C, Fig. 5) which does not transform into $MoO_2(OH)_2$ (in Eq. 7) remained at the surface (81.8%, Table 3). It is worth to note that residual MoO_3 oxide exists in a crystalline phase since the corresponding E_g value (2.85 eV, Table 7) is close to the one obtained for pure crystalline α-MoO_3 (2.88 eV, Table 7).

Following the impregnation of the dehydrated zeolite with $MoCl_5/CCl_4$ solution at 70 °C, $MoCl_5$ is transformed into $MoOCl_{4(s)}$ in the presence of certain degree of moisture (see the evolvement of H_2O between room temperature and 50 °C, red curve in Fig. 1). However, $MoOCl_{4(s)}$ evaporates during the thermal post-treatment (precisely between 70 and 200 °C based on the TA/MS results obtained with pure $MoCl_5$ [22]) and reacts with the zeolite. Due to the absence of H_2O in the medium, the transformation of $MoOCl_{4(g)}$ into MoO_3 (see page 275 in Ref. [22]) during the thermal activation is less-extended and the percentage of MoO_3 in Mo-IMP solid is therefore low (6%, Table 8). Additionally, the transformation of MoO_3 and H_2O into $MoO_2(OH)_2$ (Eq. 7) is excluded and therefore the Mo weight loss is low (10%, Table 1). The exchange of Mo by impregnation led to the expansion of the zeolite unit-cell (^{27}Al MAS NMR and XRD results, Tables 4 and 5) upon the departure of CCl_4 guest molecules. However, following the exchange, very low amounts (8.4 µmol g^{-1}, Table 8) of dimeric species were stabilized over Mo-IMP solid which corroborates the moderate decrease (from 100 to 54%) in the percentage of strong acid sites (Fig. 7 and Table 6). Theoretically, the condensation of a Mo monomer with another one to form Mo dimer is disfavoured due to the unit-cell expansion, and therefore, Mo-IMP solid stabilized very high amounts of monomeric Mo (504 µmol g^{-1}, 92%, Table 8) reduced under H_2 at 595 °C (Fig. 5). It is important to note that the formation of monomeric species over Mo-IMP solid led to the consumption of Si–OH groups (see the attenuation of the DRIFTS band's intensity at 3731 cm^{-1}, Fig. 8) following a mechanism previously described [9].

The residual MoO_3 over Mo-IMP solid (31.3 µmol g^{-1}, 6%, Table 8), reduced under H_2 at 495 °C (Fig. 5), occupied the zeolite channels (micropore blocking effect is 0.74 vs. 0.82 for Mo-SSIE, Table 2). On the other hand, this oxide phase was stabilized in amorphous state due to the discrepancy between E_g values obtained with Mo-IMP solid and crystalline α-MoO_3 (2.97 and 2.88 eV, respectively, Table 7).

During the sublimation, $MoCl_5$ is transformed into $MoOCl_{4(s)}$ in the presence of some moisture (probably retained during tarring). Nevertheless, the evaporation of $MoOCl_{4(s)}$ occurred between 70 and 550 °C and extended for 12 h, leading to a very high metal loss (76%, Table 1). The exchange of $MoOCl_{4(g)}$ in the solid–gas interface led to the consumption of 64% of Brønsted acid sites (Table 6) and to the formation of 15.1 µmol g^{-1} of $[Mo_2O_7]^{2-}$ species (i.e. 10%, Table 8). Besides dimeric species, 77% of the total Mo content over Mo-SUB solid exists in the form of $[MoO_4]^{2-}$ though the corresponding reduction feature is not distinguishable (Fig. 5) due to the strong interactions established with the support (E_g ($[MoO_4]^{2-}$) = 5.90 vs. 5.33 eV for Mo-IMP solid, Table 7) and its low concentration (122.0 vs. 504.0 µmol g^{-1} for Mo-IMP solid, Table 8).

Owing to the absence of H_2O in the atmosphere, Mo-SUB solid stabilized low amounts of crystalline MoO_3 (18.6 µmol g^{-1}, Table 8) reduced under H_2 at 450 °C (Fig. 5).

In the case of Mo-CVD solid, $Mo(CO)_6$ losses carbonyl ligands (Eq. 21) during the thermal treatment, but the presence of H_2O issued from the zeolite led to the formation of significant amounts of MoO_3 (126 µmol g^{-1}, Table 8) at the near-surface (71.2%, Table 3). These results would explain the significant micropore blocking effect over Mo-CVD solid (0.63, Table 2) when compared with Mo-SSIE (0.82, Table 2) which loaded 81.2% of MoO_3 at the surface. Additionally, MoO_3 oxide exists in amorphous state (Mo-CVD and Mo-IMP solids exhibit the same E_g value, Table 6) and was reduced under H_2 at 470 °C (Fig. 5).

Apart from the MoO_3 oxide phase, Mo-CVD solid stabilized 75 µmol g^{-1} (36%) of dimeric species (Table 8) which consumed 61% of the Brønsted acidic sites (Fig. 7 and Table 6). Nevertheless, the reduction of these species under H_2 is not detected (Fig. 5) as they established very strong interactions with the support (E_g ($[Mo_2O_7]^{2-}$) = 4.72 vs. 4.20 eV for Mo-SSIE solid, Table 7).

The differences between the catalytic properties of Mo-P catalysts are noticeable. However, in this section we will only discuss the TOF and some specific selectivity values obtained at 500 °C. In effect, ethane ammoxidation (Eq. 1) is a very complex process in which three distinct steps overlap (Eqs. 15–17). Firstly, Mo-CVD and Mo-SSIE catalysts exhibited quasi-similar percentages of Mo species as well as quasi-similar TOF values towards C_2H_4 formation (0.40 and 0.38 s^{-1}, Table 10). On the other hand, the selectivity towards C_2H_4 does not differ significantly (13 and 9%, Table 9), while the selectivity towards CO_2 is different. Apparently, for these two catalysts, the reaction expressed by Eq. 15 was successfully catalysed over dimeric Mo. Nevertheless, C_2H_4 molecules issued from Eq. 15 were successfully transformed into ethylamine (Eq. 16) and then into acetonitrile (Eq. 17) over Mo-SSIE, while amorphous MoO_3 oxide catalyses the secondary reaction over Mo-CVD catalyst, leading to higher selectivity towards CO_2 (45% vs. 4% over Mo-SSIE, Table 9).

For Mo-SUB catalyst, the activity towards C_2H_4 is very high essentially due to the presence of dimeric (TOF ($[Mo_2O_7]^{2-}$) = 4.11 s^{-1}, Table 10) and monomeric Mo (TOF ($[MoO_4]^{2-}$) = 0.51 s^{-1}, Table 10). In fact, over this catalyst, the contribution of monomeric Mo in ethane activation (Eq. 15) is more significant than that of crystalline MoO_3 (E_g = 2.84 eV, Table 7). This point is confirmed by the fact that Mo-SSIE loaded higher amount of crystalline MoO_3 than Mo-SUB (158.0 vs. 18.6 µmol g^{-1}, E_g = 2.85 eV) but exhibited lower ethylene activity (0.30 vs. 0.62 µmol s^{-1} g^{-1}, Table 9).

Despite the higher activity towards ethylene, Mo-SUB solid exhibited low Ac_{CH_3CN} value (1.18 µmol s^{-1} g^{-1}, Table 9) evidencing that Eqs. 16 and 17 are less displaced to right side. Indeed, the very high E_g($[MoO_4]^{2-}$) value (5.90 eV, Table 7) indicates that monomeric species are strongly anchored to the support which discourages the ethylene desorption upon ethane oxidative dehydrogenation (Eq. 15). On the other hand, Mo-SUB solid is less acidic (0.07 and 0.04 mmol NH_3 g^{-1}, respectively, for medium and strong acidity, Table 6), and therefore, the adsorption of NH_3 in Eq. 16 is less extended.

In the case of Mo-IMP catalyst, C_2H_6 was moderately converted into C_2H_4 (activity towards ethylene = 0.25 µmol s^{-1} g^{-1}, Table 9) despite the presence of higher amounts of monomeric species (504 = µmol g^{-1}, Table 8). However, amorphous MoO_3 transforms a fraction of C_2H_6 into CO_2 (S_{CO_2} = 20%, Table 9), and due to the lack of dimeric species (8.4 µmol g^{-1}, Table 8), a fraction of C_2H_4 issued from Eq. 15 would also be oxidized into CO_2. The ethylene molecules which were able to react with ammonia in Eq. 16 transform into AN in Eq. 17. The expansion of the unit cell would inhibit the interactions between ethylamine molecules and improves therefore the AN formation (S_{CH_3CN} = 72%, Table 9).

Conclusions

In this study, Mo/ZSM-5 zeolite catalysts were prepared, characterized and tested in ethane ammoxidation into acetonitrile at 500 °C and at a very low contact time (80 m*s*). Different protocols were adopted for the preparation of the different solids by taking into account the dehydration degree of NH_4^+-ZSM-5 zeolite. In terms of catalytic activity, the prepared materials could be classified as follows: sublimation of $MoCl_5$ (TOF = 8.78 s^{-1}) > solid-state ion exchange (TOF = 3.80 s^{-1}) > sublimation of $Mo(CO)_6$ (TOF = 1.28 s^{-1}) > impregnation (TOF = 0.44 s^{-1}). For sublimation, the use of $MoCl_5$ and dehydrated zeolite sample inhibited the formation of the inefficient MoO_3 in amorphous state which catalyses the hydrocarbon(s) combustion into CO_2. However, the lack of H_2O in the impregnation medium avoided the Mo weight loss, which enhanced the grafting of monomeric species into silanol groups at the detriment of active $[Mo_2O_7]^{2-}$ species formation. Using hydrated ZSM-5 sample, the sublimation of $Mo(CO)_6$ and the exchange of $MoCl_5$ in the solid state led to quasi-similar percentages of MoO_3 and dimeric Mo. Nevertheless, the formation of amorphous MoO_3 during the sublimation of $Mo(CO)_6$ deteriorates the catalytic activity. Whatever the used method, the different prepared materials stabilized very low amounts of heptameric Mo which does not contribute to ethane ammoxidation into acetonitrile.

Acknowledgements This work is dedicated to the memory of Professor Farhat Farhat (Faculté de Pharmacie de Monastir, Tunisie), a great educator in the field of analytical chemistry and the memory of Professor Mohamed Salah Belkhiria (Faculté des Sciences de Monastir, Tunisie), a talented educator of a great knowledge in the field of coordination chemistry.

References

1. Global acetonitrile market to reach 143 Kilotons by 2024 (CAGR 4%). https://www.abnewswire.com/pressreleases/global-acetonitrile-market-to-reach-143-kilotons-by-2024-cagr-4_400673.html. Accessed 26 June 2019
2. O.B. Rudakov, L.V. Rudakova, V.F. Selemenev, Acetonitrile as tops solvent for liquid chromatography and extraction. J. Anal. Chromatogr. Spectrosc. **1**, 1–19 (2018). https://doi.org/10.24294/jacs.v1i2.883
3. M.M. Miller, A.J. DelMonte, Chapter 6.2: Six-membered ring systems: diazines and benzo derivatives. Prog. Heterocycl. Chem. **23**, 371–402 (2011). https://doi.org/10.1016/B978-0-08-096805-6.00013-9
4. J.-F. Cote, D. Brouillette, J.E. Desnoyers, J.-F. Rouleau, J.-M. St-Arnaud, G. Perron, Dielectric constants of acetonitrile, gamma-butyrolactone, propylene carbonate, and 1,2-dimethoxyethane as a function of pressure and temperature. J. Solut. Chem. **25**, 1163–1173 (1996). https://doi.org/10.1007/BF00972644
5. N.D. Tring, D. Lepage, D. Aymé-Perrot, A. Badia, M. Dollé, D. Rochefort, An artificial lithium protective layer that enables the use of acetonitrile-based electrolytes in lithium metal batteries. Angew. Chem. Int. Ed. **57**, 5072–5075 (2018). https://doi.org/10.1002/anie.201801737
6. E.L. Tollefson, R.M. Decker, C.B. Johnson, Development of a process for production of acetonitrile from acetic acid and ammonia. Can. J. Chem. Eng. **48**, 219–223 (1970). https://doi.org/10.1002/cjce.5450480223
7. A. Tripodi, E. Bahadori, D. Cespi, F. Passarini, F. Cavani, T. Tabanelli, I. Rossetti, Acetonitrile from bioethanol ammoxidation: process design from the grass-roots and life cycle analysis. ACS Sustain. Chem. Eng. **6**, 5441–5451 (2018). https://doi.org/10.1021/acssuschemeng.8b00215
8. F. Ayari, M. Mhamdi, J. Alvarez-Rodriguez, A.R. Guerrero-Ruiz, G. Delahay, A. Ghorbel, Cr-ZSM-5 catalysts for ethylene ammoxidation: effects of precursor nature and Cr/Al molar ratio on the physicochemical and catalytic properties. Microporous Mesoporous Mater. **171**, 166–178 (2013). https://doi.org/10.1016/j.micromeso.2012.12.026
9. E. Mannei, F. Ayari, C. Petitto, E. Asedegbega-Nieto, A.R. Guerrero-Ruiz, G. Delahay, M. Mhamdi, A. Ghorbel, Light hydrocarbons ammoxidation into acetonitrile over Mo-ZSM-5 catalysts: effect of molybdenum precursor. Microporous Mesoporous Mater. **241**, 246–257 (2017). https://doi.org/10.1016/j.micromeso.2016.12.021
10. F. Veatch, J. L. Callahan, E. C. Milberger, R. W. Foreman, in *Proceedings of the 2nd International Congress on Catalysis*, New York, 1960, vol. 2, p. 2647
11. J.F. Brazdil, M.A. Toft, *Encyclopedia of Catalysis, Ammoxidation* (Wiley, Hoboken, 2010), pp. 1–62. https://doi.org/10.1002/0471227617.eoc020
12. S. Essid, F. Ayari, R. Bulánek, J. Vaculík, M. Mhamdi, G. Delahay, A. Ghorbel, Over- and low-exchanged Co/BEA catalysts: general characterization and catalytic behaviour in ethane ammoxidation. Catal. Today **304**, 103–111 (2018). https://doi.org/10.1016/j.cattod.2017.08.027
13. S. Essid, F. Ayari, R. Bulánek, J. Vaculík, M. Mhamdi, G. Delahay, A. Ghorbel, Improvement of the conventional preparation methods in Co/BEA zeolites: characterization and ethane ammoxidation. Solid State Sci. **93**, 13–23 (2019). https://doi.org/10.1016/j.solidstatesciences.2019.04.008
14. E. Mannei, F. Ayari, E. Asedegbega-Nieto, M. Mhamdi, G. Delahay, Z. Ksibi, A. Ghorbel, Physicochemical and catalytic properties of over- and low-exchanged Mo-ZSM-5 ammoxidation catalysts. Chem. Paper **73**, 619–633 (2019). https://doi.org/10.1007/s11696-018-0617-1
15. F. Solymosi, A. Cserenyi, A. Szoke, T. Bansagi, A. Oszko, Aromatization of methane over supported and unsupported Mo-based catalysts. J. Catal. **165**, 150–161 (1997). https://doi.org/10.1006/jcat.1997.1478
16. J.R. Johns, R.F. Howe, Preparation of molybdenum mordenite from $MoCl_5$. Zeolites **5**, 251–256 (1985). https://doi.org/10.1016/0144-2449(85)90096-X
17. R.F. Howe, J. Ming, W.S. Tin, Z.J. Hua, Comparison of zeolites and aluminophosphates as hosts for transition metal complexes. Catal. Today **6**, 113–122 (1989). https://doi.org/10.1016/0920-5861(89)85013-8
18. Y. Xu, S. Liu, X. Guo, L. Wang, M. Xie, Methane activation without using oxidants over Mo/HZSM-5 zeolite catalysts. Catal. Lett. **30**, 135–149 (1994). https://doi.org/10.1007/BF00813680
19. D. Wang, J.H. Lunsford, M.P. Rosynek, Characterization of a Mo/ZSM-5 catalyst for the conversion of methane to benzene. J. Catal. **169**, 347–358 (1997). https://doi.org/10.1006/jcat.1997.1712
20. G. Dantsin, K.S. Suslick, Sonochemical preparation of a nanostructured bifunctional catalyst. J. Am. Chem. Soc. **122**, 5212–5214 (2000). https://doi.org/10.1021/ja994300w
21. A.K. Galway, Melting and thermal decompositions of solids. An appraisal of mechanistic interpretations of thermal processes in crystals. J. Therm. Anal. Calorim. **87**, 601–615 (2007). https://doi.org/10.1007/s10973-006-7529-y
22. F. Ayari, E. Mannei, E. Asedegbega-Nieto, M. Mhamdi, A.R. Guerrero-Ruiz, G. Delahay, A. Ghorbel, Elucidation of the solid-state ion exchange mechanism of $MoCl_5$ into ZSM-5 zeolite. Thermochim. Acta **655**, 269–277 (2017). https://doi.org/10.1016/j.tca.2017.07.011
23. J.J. Cruywagen, Protonation, oligomerization, and condensation reactions of vanadate (V), molybdate (VI), and tungstate (VI). Adv. Inorg. Chem. **49**, 127–182 (2000). https://doi.org/10.1016/S0898-8838(08)60270-6
24. F. Ayari, E. Mannei, E. Asedegbega-Nieto, M. Mhamdi, A.R. Guerrero-Ruiz, G. Delahay, A. Ghorbel, Solid–state ion exchange of ammonium heptamolybdate tetrahydrate into ZSM-5 zeolite. J. Therm. Anal. Calorim. **131**, 1295–1306 (2018). https://doi.org/10.1007/s10973-017-6545-4
25. S.D. Djajanti, R.F. Howe, MOCVD in Zeolites using $Mo(CO)_6$ and $W(CO)_6$ as precursors. Stud. Surf. Sci. Catal. **97**, 197–204 (1995). https://doi.org/10.1016/S0167-2991(06)81890-2
26. J.-H. Park, T.S. Sudarshan, *Chemical Vapor Deposition*, vol. 2, Surface engineering series (ASM International, Cleveland, 2001), p. 3
27. A. Antiñolo, P. Cañizares, F.C. Hermosilla, J.F. Baeza, F.J. Fúnez, A. de Lucas, A. Otero, L. Rodríguez, J.L. Valverde, A grafted methane partial oxidation catalyst from $MoO_2(acac)_2$ and HZSM-5 zeolite. Appl. Catal. A: Gen. **193**, 139–146 (2000). https://doi.org/10.1016/S0926-860X(99)00423-8
28. Q. Guo, L. Li, L. Chen, Y. Wang, S. Ren, B. Shen, Benzylation of anisole catalyzed by $MoCl_5$ or $MoCl_5$/molecular sieve system. Energy Fuels **23**, 51–54 (2009). https://doi.org/10.1021/ef800680p
29. E. Mannei, F. Ayari, E. Asedegbega-Nieto, M. Mhamdi, A.R. Guerrero-Ruiz, G. Delahay, A. Ghorbel, Solid-state ion exchange of molybdenum (VI) acetylacetonate into ZSM-5

zeolite. Thermochim. Acta **652**, 150–159 (2017). https://doi.org/10.1016/j.tca.2017.03.020
30. F. Ayari, E. Mannei, E. Asedegbega-Nieto, M. Mhamdi, A.R. Guerrero-Ruiz, G. Delahay, A. Ghorbel, More insight on the isothermal spreading of solid MoO_3 into ZSM-5 zeolite. React. Kinet. Mech. Catal. **124**, 419–436 (2018). https://doi.org/10.1007/s11144-018-1357-5
31. Y. Song, C. Sun, W. Shen, L. Lin, Hydrothermal post–synthesis of HZSM-5 zeolite to enhance the coke–resistance of Mo/HZSM-5 catalyst for methane dehydroaromatization reaction: reconstruction of pore structure and modification of acidity. Appl. Catal. A: Gen. **317**, 266–274 (2007). https://doi.org/10.1016/j.apcata.2006.10.037
32. R.W. Borry, Y.H. Kim, A. Huffsmith, J.A. Reimer, E. Iglesia, Structure and density of Mo and acid sites in Mo-exchanged H-ZSM5 catalysts for nonoxidative methane conversion. J. Phys. Chem. B **103**, 5787–5796 (1999). https://doi.org/10.1021/jp990866v
33. E. Oldfield, J. Haase, K.D. Schmitt, S.E. Schramm, Characterization of zeolites and amorphous silica-aluminas by means of aluminum-27 nuclear magnetic resonance spectroscopy: a multifield, multiparameter investigation. Zeolites **14**, 101–109 (1994). https://doi.org/10.1016/0144-2449(94)90003-5
34. E. Lippmaa, A. Samoson, M. Mägi, High-resolution aluminum–27 NMR of aluminosilicates. J. Am. Chem. Soc. **108**, 1730–1735 (1986). https://doi.org/10.1021/ja00268a002
35. M.B. Rao, R.G. Jenkins, Molecular dimensions and kinetic diameters for diffusion for various species. Carbon **25**, 445–446 (1987). https://doi.org/10.1016/0008-6223(87)90018-2
36. F.S. Xiao, S. Zheng, J. Sun, R. Yu, S. Qiu, R. Xu, Dispersion of inorganic salts into zeolites and their pore modification. J. Catal. **176**, 474–487 (1998). https://doi.org/10.1006/jcat.1998.2054
37. C.A. Fyfe, G.J. Kennedy, C.T. De Schutter, G.T. Kokotailo, Sorbate-induced structural changes in ZSM-5 (silicalite). J. Chem. Soc. Chem. Commun. (1984). https://doi.org/10.1039/C39840000541
38. Y. Marcus, *The Properties of Solvents*, vol. 4 (Wiley, England, 1999), p. 239
39. D.C. Baertsch, H.H. Funke, J.L. Falconer, R.D. Noble, Permeation of aromatic hydrocarbon vapors through silicalite–zeolite membranes. J. Phys. Chem. **100**, 7676–7679 (1996). https://doi.org/10.1021/jp960226h
40. K.G. Marek, K. Tarach, M. Choi, 2,6-di-tert-butylpyridine sorption approach to quantify the external acidity in hierarchical zeolites. J. Phys. Chem. C **118**, 12266–12274 (2014). https://doi.org/10.1021/jp501928k
41. J. Goetze, I. Yarulina, J. Gascon, F. Kapteijn, B.M. Weckhuysen, Revealing lattice expansion of small-pore zeolite catalysts during the methanol-to-olefins process using combined Operando X-ray diffraction and UV–Vis spectroscopy. ACS Catal. **8**, 2060–2070 (2018). https://doi.org/10.1021/acscatal.7b04129
42. M. Niwa, M. Iwamoto, K. Segawa, Temperature-programmed desorption of ammonia on zeolites. Influence of the experimental conditions on the acidity measurement. Bull. Chem. Soc. Jpn. **59**, 3735–3739 (1986). https://doi.org/10.1246/bcsj.59.3735
43. P. Sarv, C. Fernadez, J.-P. Amoureux, K. Keskinen, Distribution of tetrahedral aluminium sites in ZSM-5 type zeolites: an ^{27}Al (Multiquantum) Magic Angle Spinning NMR Study. J. Phys. Chem. **100**, 19223–19226 (1996). https://doi.org/10.1021/jp962519g
44. G.A. Khan, C.A. Hogarth, Optical absorption spectra of evaporated V_2O_5 and co-evaporated V_2O_5/B_2O_3 thin films. J. Mater. Sci. **26**, 412–416 (1991). https://doi.org/10.1007/BF00576535
45. R.S. Weber, Effect of local structure on the UV-visible absorption edges of molybdenum oxide clusters and supported molybdenum oxides. J. Catal. **151**, 470–474 (1995). https://doi.org/10.1006/jcat.1995.1052
46. L. Čapek, J. Dědeček, P. Sazama, B. Wichterlová, The decisive role of the distribution of Al in the framework of beta zeolites on the structure and activity of Co ion species in propane-SCR-NOx in the presence of water vapour. J. Catal. **272**, 44–54 (2010). https://doi.org/10.1016/j.jcat.2010.03.013
47. D. Kaucký, A. Vondrová, J. Dědeček, B. Wichterlová, Activity of Co ion sites in ZSM-5, Ferrierite, and Mordenite in selective catalytic reduction of NO with methane. J. Catal. **194**, 318–329 (2000). https://doi.org/10.1006/jcat.2000.2925
48. E. Mannei, F. Ayari, M. Mhamdi, M. Almohalla, A.R. Guerrero-Ruiz, G. Delahay, A. Ghorbel, Ammoxidation of C2 hydrocarbons over Mo-zeolite catalysts prepared by solid-state ion exchange: nature of molybdenum species. Microporous Mesoporous Mater. **219**, 77–86 (2016). https://doi.org/10.1016/j.micromeso.2015.07.036
49. P. Krüger, M. Petukhov, B. Domenichini, A. Berkó, S. Bourgeois, Monolayer formation of molybdenum carbonyl on Cu(111) revealed by scanning tunneling microscopy and density functional theory. J. Phys. Chem. C **116**, 10617–10622 (2012). https://doi.org/10.1021/jp300832a